

Separation of Infrared and Bulk in Thermal QCD

Xiao-Lan Meng^{1,2}, Peng Sun³, Andrei Alexandru⁴, Ivan Horváth^{5,6}, Keh-Fei Liu^{6,7}, Gen Wang⁸, and Yi-Bo Yang^{1,2,9,10}



(χ QCD & CLQCD Collaboration)

¹CAS Key Laboratory of Theoretical Physics, Institute of Theoretical Physics, Chinese Academy of Sciences, Beijing 100190, China

²University of Chinese Academy of Sciences, School of Physical Sciences, Beijing 100049, China

³Institute of Modern Physics, Chinese Academy of Sciences, Lanzhou, 730000, China

⁴The George Washington University, Washington, DC 20052, USA

⁵Nuclear Physics Institute CAS, 25068 Rez (Prague), Czech Republic

⁶University of Kentucky, Lexington, KY 40506, USA

⁷Nuclear Science Division, Lawrence Berkeley National Laboratory, Berkeley, California 94720, USA

⁸Aix-Marseille Université, Université de Toulon, CNRS, CPT, Marseille, France

⁹School of Fundamental Physics and Mathematical Sciences, Hangzhou Institute for Advanced Study, UCAS, Hangzhou 310024, China

¹⁰International Centre for Theoretical Physics Asia-Pacific, Beijing/Hangzhou, China

New thermal phase of QCD, featuring scale invariance in the infrared (IR), was proposed to exist both in the pure-gluon ($N_f=0$) and the “real-world” ($N_f=2+1$) settings. Among key aspects of the proposal is that the system in this *IR phase* separates into two independent components: the scale-invariant IR part and the non-invariant bulk. Such scenario requires non-analyticities in the theory and, in case of pure-gluon QCD, they were found to arise via Anderson-like mobility edges in Dirac spectra ($\lambda_{\text{IR}}=0, \pm\lambda_A \neq 0$) manifested in dimension function $d_{\text{IR}}(\lambda)$. Here we present first evidence that this mechanism is also at work in “real-world QCD” ($N_f=2+1$ theory at physical quark masses and $a=0.105$ fm), supporting the existence of the proposed IR regime. Indeed, at $T=234$ MeV, we find the dimensional jump between zero modes and lowest near-zero modes very close to unity ($d_{\text{IR}}=3$ to $d_{\text{IR}}\simeq 2$), exactly like in pure-gluon QCD in IR phase. However, no jump is found at $T=187$ MeV which is in the intermediate region between chiral crossover at $T_c \approx 155$ MeV and the onset T_{IR} of IR phase, originally estimated at $200 < T_{\text{IR}} < 250$ MeV.

1. Introduction: Starting with the pre-QCD times of Hagedorn [1, 2] and early lattice QCD calculations in the pure-gluon setting [3–5], the question of thermal transition in strongly-interacting matter has become one of the highly researched topics in nuclear and particle physics. Apart from well-motivated need to understand strong interactions, the interest in the issue was fueled, to a large extent, by the potential significance of its resolution to the physics of early universe.

Hagedorn in fact set the basic scenario, wherein the thermal transformation process in strong interactions boils down to a single “instability temperature” which, nowadays in QCD, is commonly referred as the critical temperature (T_c). Due to the non-perturbative nature of the problem, lattice QCD became the workhorse for investigations in this area. Advances in lattice QCD techniques and computational resources led to a major conclusion, namely that true phase transition does not occur in “real-world” QCD. Rather, an analytic crossover takes place in the temperature range 150–200 MeV, with $T_c \approx 155$ MeV for the case of chiral crossover [6].

Transitionless outlook meant a setback to QCD’s role

in cosmology, but an important new twist appeared around the same time. Experiments at RHIC and LHC concluded that the state of strongly interacting matter with properties akin to near-perfect fluid exists in certain range of temperatures [7–11]. Among other things, this invites questions about how can such an exotic state of matter arise without a true phase transition.

To this end, some of us presented evidence of an unusual change in QCD Dirac spectra at temperatures well above the chiral crossover [12]: the anomalous accumulation of infrared (IR) Dirac modes, first seen in high- T phase of pure-gluon QCD [13] and shown to persist into the continuum and infinite-volume limits [14], dramatically increases and starts to exhibit signs of scale-invariant behavior. This sharp change was found in both the pure-gluon and real-world ($N_f=2+1$ at physical masses) QCD [12]. It was proposed that, at the associated temperature T_{IR} , thermal state of strong interactions reconfigures by forming two independent components separated by new scale $\Lambda_{\text{IR}}(T) \lesssim T$: the bulk governing distances $\ell < 1/\Lambda_{\text{IR}}$ and the IR part describing $\ell > 1/\Lambda_{\text{IR}}$ via scale-invariant glue [12]. In pure-gluon case, T_{IR} coincides

with T_c of Polyakov-line phase transition. In real-world QCD, it was also proposed to be a true phase transformation occurring at $200 < T_{\text{IR}} < 250$ MeV [12]. Its presence may clarify the physics of near-perfect fluid and enhance the role of “QCD transition” in cosmology.

Although the proposed phase transition is symmetry-based, it is very unusual: the anomalously broken scale invariance of glue fields gets restored, but only in IR sector/component of the theory. This is sufficient to predict massless behavior in glue [12], but the associated long-distance physics only becomes important at volumes unusually large by normal QCD standards. In fact, obtaining insights into this emerging IR world via numerical simulations needs somewhat unusual techniques [15, 16].

The 2-component scenario was first evoked by a clean IR-bulk separation in Dirac spectra (bimodality of mode density $\rho(\lambda)$), which is very suggestive of decoupling [12]. But more detail was needed. Indeed, how would the scale invariant and non-invariant physics coexist and would it imply a non-analytic running of the coupling constant at Λ_{IR} ? Concrete proposal was presented in Refs. [15, 16], ascribing the origin of non-analyticity to two Anderson-like mobility edges (critical points) in Dirac spectra. The first one at $\lambda_A > 0$ was found previously [17–21], and its purpose here is to shield the IR component from the influence of the bulk. Indeed, bulk fluctuations (including UV) will not affect the IR component owing to the intervening non-analyticity. The second mobility edge was found recently [16], and is strictly IR ($\lambda_{\text{IR}} = 0$). Its role is to facilitate the long-range physics of the IR component.

A suitable tool to express this scenario is the function $d_{\text{IR}}(\lambda)$, namely the spatial IR dimension of Dirac modes at eigenvalue λ [15]. Indeed, d_{IR} is a proper dimensional construct to probe the infrared [22]. The key conceptual step granting its uses in quantum theory is the assignment of a meaningful measure-based dimension to a region *effectively selected* by probabilities. This has recently become possible via effective number theory [23–25]: replacement of ordinary counting in definition of box-counting dimension for fixed sets by effective counting for probability distributions leads to such measure-based dimension [22]. For Dirac modes in thermal QCD the prescription is as follows. In lattice-regularized Euclidean setup the number of sites $N(L) \equiv (L/a)^3/(aT)$ (UV cutoff $1/a$, IR cutoff $1/L$, temperature T) grows as L^3 at fixed a , conveying that IR dimension of space is $D_{\text{IR}} = 3$. But Dirac eigenmode $D\psi(x) = \lambda\psi(x)$ entails probabilities $P = (p_1, p_2, \dots, p_N)$, $p_i \equiv \psi^+(x_i)\psi(x_i)$, and sites have to be counted effectively in order to quantify the volume ψ actually extends into, namely [23]

$$N \longrightarrow N_\star[\psi] = N_\star[P] = \sum_{i=1}^N \min\{Np_i, 1\} \quad (1)$$

The IR scaling of QCD-averaged effective volume at given λ then determines $d_{\text{IR}}(\lambda)$ at UV cutoff a , namely [15, 22]

$$\langle N_\star \rangle_{L,\lambda,a} \propto L^{d_{\text{IR}}(\lambda,a)} \quad \text{for } L \rightarrow \infty \quad (2)$$

TABLE I. UV cutoff a , pion mass m_π , lattice volumes $n_L^3 \times n_T$ and temperature T of lattice QCD ensembles studied.

$a(\text{fm})$	$m_\pi(\text{MeV})$	n_L	n_T	$T(\text{MeV})$
0.105	135	24/28/32/40/48/64/96	8	234
0.105	135	32/40/48/64	10	187

Using the overlap Dirac operator due to its superior chiral and topological properties, an unusual $d_{\text{IR}}(\lambda)$ was found in IR phase of pure-gluon QCD [12]. Indeed, the function is non-analytic at both λ_{IR} and λ_A , with spectral region of low- d ($d_{\text{IR}} \leq 1$) modes between them [15]. Moreover, in contrast to exact zero modes, which are $d_{\text{IR}} = 3$, the lowest near-zero modes ($\lambda \rightarrow 0^+$) are close to other topological value $d_{\text{IR}} = 2$. Such jump at $\lambda_{\text{IR}} = 0$ is surprising since the proposed origin of anomalous IR mode accumulation is the conventional mixing of topological lumps [13, 26] which, in absence of additional (unknown) effects, leads to $d_{\text{IR}} = 3$ in both cases. The jump could thus offer valuable clues on IR phase dynamics, and could be used to detect the transition into IR phase.

In this work, we make a key step toward this proposal becoming a reality: we present evidence supporting the existence of the above unusual pattern also in “real-world QCD”. Indeed, in $N_f = 2 + 1$ theory with physical quark masses we find at $T = 234$ MeV and 187 MeV

$$234 \text{ MeV} : \quad d_{\text{IR}}(0) = 2.98(09) \quad d_{\text{IR}}(0^+) = 2.03(16) \quad (3)$$

$$187 \text{ MeV} : \quad d_{\text{IR}}(0) = 2.96(22) \quad d_{\text{IR}}(0^+) = 3.03(31) \quad (4)$$

with identical UV cutoffs $a = 0.105$ fm. Eq. (3) suggests that QCD at $T = 234$ MeV is in IR phase. It also supports the topological origin of IR-phase dynamics [15, 16] (see also [13, 26, 27]) and strengthens its connection to non-analyticities of Anderson-like origin [16]. In fact, the topology aspects may have close ties to critical Anderson dynamics [28–30] which is entirely unexpected. Eq. (4) confirms that there is a temperature range above the chiral crossover $T_c \approx 155$ MeV but below the onset T_{IR} of IR phase ($200 < T_{\text{IR}} < 250$ MeV [12]) where there is no non-analyticity of $d_{\text{IR}}(\lambda, T)$ near $\lambda = 0$. It is only above T_{IR} that the non-analyticity (and the IR phase itself) emerges [12, 15, 16].

2. *Numerical setup and Dirac spectral density:* We lattice-regularize $N_f = 2 + 1$ QCD using tadpole-improved clover fermion action (1-step stout link smearing with parameter 0.125) and tadpole-improved Symanzik gauge action at $a = 0.105$ fm and $m_\pi \simeq 135$ MeV. Ensembles at temperatures $T = 187$ and 234 MeV on numerous spatial volumes (up to $L = 10.1$ fm) were generated by CLQCD collaboration (see Table I), which allows for calculation of IR dimensions. More detailed ensemble description is given in Ref. [31]. We note in passing that ensembles with similar quark and gauge actions were already used in previous zero-temperature calculations [31–35].

Lattice glue fields U in these theories will be studied via their effect on the overlap Dirac operator $D_{\text{ov}}[U]$. We construct D_{ov} using the original square-root prescription [36] at $\rho = 1.5$ with 1-step HYP smearing of U . To

determine the low-lying eigensystem, we select the chiral sector containing zero mode(s), calculate the eigenvectors of $D_{\text{ov}}^\dagger D_{\text{ov}}$ in it using the Arnoldi method, and then construct non-zero modes [37–40]. Transformation $D \equiv D_{\text{ov}} / (1 - \frac{a}{2\rho} D_{\text{ov}})$ [41] yields purely imaginary eigenvalues ($D\psi_\lambda(x) = i\lambda\psi_\lambda(x)$) and the associated spectral density is $\rho(\lambda) = T \sum_i \delta(\lambda - \lambda_i) / L^3$. Further technical details can be found in Appendix A.

Eigenmodes with λ up to ≈ 500 MeV were computed for ensembles in Table I. Densities $\rho(\lambda)$ were calculated and renormalized in $\overline{\text{MS}}$ at 2 GeV, using $Z_m = Z_S^{-1} = 0.907(26)$ obtained by interpolating the results at 11 UV cutoffs [42]. Our main interest is the temperature range $200 < T < 250$ MeV, where the system was originally predicted to reach the IR phase at certain T_{IR} . In Fig. 1 we show $\rho(\lambda)$ at $T = 234$ MeV (red circles). The striking bimodal structure exhibits features previously associated with IR phase [12], including a fully-formed region of mode depletion: the plateau. For comparison, we also show densities at $T = 187$ MeV (green crosses and $T \approx 0$ MeV (black triangles)). The three simulations were performed in the same lattice setup and at identical parameters except for $n_T = 8, 10, 96$ respectively, which controls the temperature. The changes in the displayed sequence of Dirac spectra are thus exclusively due to the changing level of thermal agitation. In fact, the three cases illustrate three thermal regimes of Ref. [12] in terms of IR-bulk separation. Indeed, the $T \approx 0$ case showcases the domain $0 \leq T < T_A$ ($T_A \approx T_c \approx 155$ MeV) where IR and bulk are not meaningfully separable. At $T = 187$ MeV, the system is inside the finite transition regime $T_A < T < T_{\text{IR}}$ where the separation process effectively starts at T_A and becomes complete at T_{IR} which is the onset of IR phase. At $T = 234$ MeV, IR and bulk seem fully separated (IR phase), consistently with the original estimate $T_{\text{IR}} \in (200, 250)$ MeV [12].

Although the above reasoning based on IR-bulk separation is quite cogent, it is qualitative. Making a sharp statement about the distinction it suggests between $T = 187$ MeV (not IR phase) and 234 MeV (IR phase) requires a more quantitative approach. To that end, recall that temperature T_{IR} is defined as the onset of negative leading power in the infrared behavior of $\rho(\lambda)$ [12]. Based on the numerically verified case of pure-gluon theory, it was conjectured to coincide with temperature where IR dimension function $d_{\text{IR}}(\lambda, T)$ becomes non-analytic (discontinuous) at $\lambda = 0$ [15, 16]. Since IR dimension is a global characteristic of a mode, we expect it to be a more robust indicator of a phase change. Indeed, we will provide evidence that the qualitative distinction between $T = 187$ and 234 MeV is cleanly seen in this second non-analyticity aspect.

Before proceeding to make this point, let us comment in passing on a different aspect conveyed by Fig. 1. In particular, it is generally assumed, based on asymptotic freedom, that UV behavior of $\rho(\lambda)$ is the same at any temperature T . However, it is not a priori clear from such arguments how and at what scales this occurs. Remark-

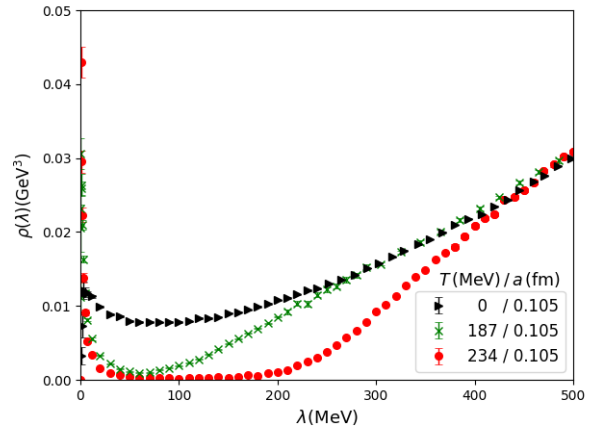


FIG. 1. Spectral density $\rho(\lambda)$ at $T \approx 0$ MeV (triangles), $T = 187$ MeV (crosses) and $T = 234$ MeV (circles). The cutoffs are $a = 0.105$ fm and $L = 5.0$ fm in all cases. At $T \approx 0$ MeV, $\rho(\lambda)$ was computed using stochastic estimates [43].

ably, we see that $\rho(\lambda, T = 187 \text{ MeV})$ not only approaches but becomes effectively indistinguishable from $\rho(\lambda, T = 0)$ at unexpectedly small $\lambda \sim 270$ MeV. Indeed, the two dependences join above the scale of temperature (187 MeV) but well before the asymptotic behavior ($\rho(\lambda) \propto \lambda^3$) sets in. System at $T = 234$ MeV follows the same pattern.

3. IR dimensions of Dirac eigenmodes: Following the reasoning in Sec. 2, we now examine in detail whether the unusual $d_{\text{IR}}(\lambda)$ in IR phase of pure-gluon QCD [15] is also manifested in real-world QCD at $T = 234$ MeV and $T = 187$ MeV. To that end, we utilize and extend the techniques of early studies. A useful concept is the “finite-volume” d_{IR} , namely [15]

$$d_{\text{IR}}(L, s) = \frac{1}{\ln(s)} \ln \frac{N_\star(L)}{N_\star(L/s)} \quad , \quad s > 0 \quad (5)$$

since then $d_{\text{IR}} = \lim_{L \rightarrow \infty} d_{\text{IR}}(L, s)$ independently of s . Estimating the limit from linear extrapolations in $1/L$ works well in Anderson models, at least for extended states and at criticality [28]. Here we utilize this, and point out that the procedure is equivalent to direct fitting of $N_\star(L)$ to the form $b L^{d_{\text{IR}}} e^{-c/L}$ (see Appendix B), which is technically more convenient.

$T = 234$ MeV. Using the data on five largest systems to fit, we obtained $d_{\text{IR}}(\lambda)$ shown in Fig. 2. Despite some differences (see below), its behavior is strikingly similar to pure-gluon case (Fig. 1 of Ref. [15]). Important commonality is the discontinuity feature at $\lambda_{\text{IR}} = 0$, suggesting that exact zero-modes ($d_{\text{IR}}(0) \simeq 3$, full red circle) differ from lowest near-zero modes ($d_{\text{IR}}(0^+) \simeq 2$, red circles) in a robust qualitative manner. This is made explicit by the inset of Fig. 2 focusing on the very deep IR, and yielding $d_{\text{IR}}(0^+) = 2.03(16)$ after linear $\lambda \rightarrow 0^+$ extrapolation. Explanation of this (more than 5σ) difference in terms of the underlying IR glue may provide important clues toward the full understanding of IR phase.

Like in pure-gluon case, we find a clear low- d plateau,

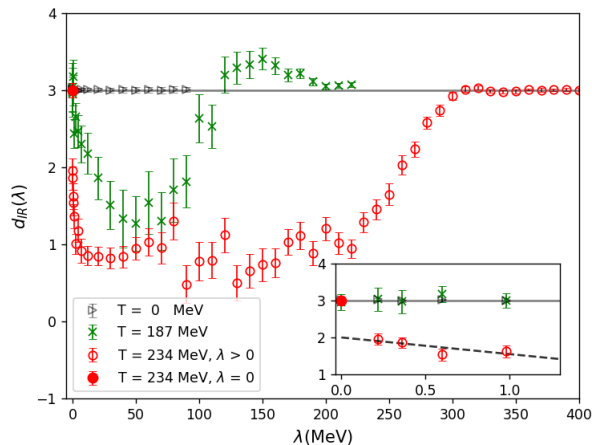


FIG. 2. Function $d_{\text{IR}}(\lambda)$ at $T = 0$ (triangles), $T = 187$ MeV (crosses) and $T = 234$ MeV (circles). The full circle is the result for exact zero modes at $T = 234$ MeV. The inset zooms in on deep infrared with linear $\lambda \rightarrow 0^+$ extrapolations shown.

here in the range of about 10–220 MeV, roughly coinciding with the region of strongly suppressed $\rho(\lambda)$ (Fig. 1 vs Fig. 2). Dimensional structure of plateaus will be further clarified in forthcoming studies using the multidimensionality technique of Ref. [30].

The onset of rise toward dimension 3 past $\lambda \approx 220$ MeV confirms the viability of scenario with mobility edges λ_{IR} and $\pm\lambda_A$ [16]. However, the discontinuity of $d_{\text{IR}}(\lambda)$ at presumed λ_A is not apparent in our data, contrary to both the pure-gluon case [15] and the situation in Anderson models [28]. Resolution of this difference may provide an additional new insight into the IR-phase dynamics.

$T = 187$ MeV. Data for all four system sizes were used in fits to obtain $d_{\text{IR}}(\lambda)$ shown in Fig. 2. Here the situation is different, most visibly in the approach to deep infrared (see the inset). In particular, we find no detectable disconnect between exact zero modes and the deepest near-zero modes. In fact, in this case we have $d_{\text{IR}}(0^+) = 3.03(31)$ after linear $\lambda \rightarrow 0^+$ extrapolation in clear contrast to $T = 234$ MeV.

The dip of $d_{\text{IR}}(\lambda)$ in the range of about 10–90 MeV is a structure qualitatively between a low- d_{IR} plateau of $T = 234$ MeV and a constant behavior typical of low temperatures. We thus cannot say unambiguously whether this aspect is IR phase-like or not. However, the moderate unphysical overshooting of $d_{\text{IR}} = 3$ above the dip and rather large error bars suggest that better statistics and simulation of somewhat larger systems will provide the soon-accessible answer to this question.

$T = 0$. It is instructive in this context to also perform a d_{IR} calculation at zero temperature. To that end, we used three 2+1 flavor Mobius+Iwasaki+DSDR ensembles from the RBC collaboration at $a = 0.194$ fm and $n_L = 24, 32, 48$ [44, 45]. With three sizes available, we performed two-parameter fits of the form $bL^{d_{\text{IR}}}$ with results shown in Fig. 2 (triangles). Note that the available range of λ is smaller due to the large number of lattice points at low temperatures. However, apparently suffi-

cient statistics and lattice sizes yield a stable $d_{\text{IR}}(\lambda) \equiv 3$, as expected.

4. *IR scaling:* To illustrate the quality of scaling in various λ -regimes shown in Fig. 2, we plot in Fig. 3 the fraction f_* of volume taken by the effective support of the state, namely $f_* \equiv N_*/N = N_*/(n_L^3 n_T)$. Since $N_*(L) \propto L^{d_{\text{IR}}} e^{-c/L}$ is used to extract d_{IR} , we have $f_*(L) \propto L^{d_{\text{IR}}-3} e^{-c/L}$ and these fits are shown in Fig. 3 for $T = 234$ MeV. The displayed χ^2/dof for modes in different regimes do indeed confirm very good scaling behavior. Note how functions $f_*(L)$ in Fig. 3 visually separate the bulk modes and near-bulk modes from IR modes. Indeed, although zero-modes are $d_{\text{IR}} = 3$, and hence occupy a finite fraction of volume in thermodynamic limit ($\lim_{L \rightarrow \infty} f_*(L) > 0$), its magnitude is much smaller than that of typical bulk modes. At the same time, for $d_{\text{IR}} < 3$ modes of IR component the effective fraction vanishes ($\lim_{L \rightarrow \infty} f_*(L) = 0$).

Fig. 3 reveals that the lowest near-zero modes we studied ($\lambda = 0.22$ MeV, $d_{\text{IR}} < 3$) have larger f_* at studied volumes than those of zero modes ($\lambda = 0$, $d_{\text{IR}} = 3$). But given their d_{IR} , this order has to reverse at sufficiently large volume. We can read off the graphs in Fig. 3 that this happens at $L \approx 20$ fm. Such deep IR thresholds simply do not appear in other QCD regimes. Only at larger L will modes at $\lambda = 0.22$ MeV become “sparser” than zero modes. Note that the qualitative difference between zero and near-zero modes is expressed here by the opposite convexity properties of their $f_*(L, \lambda)$.

Finally, we wish to gain some visual insight into the spatial geometry of modes. In definition (1) of N_* , uniform probability $p_u = 1/N$ enters as a reference value: points x_i with $p(x_i) = \psi_\lambda^\dagger(x_i)\psi_\lambda(x_i) \geq p_u$ are guaranteed to be in effective support, and we refer to them as “core”. We wish to set up a sea-level representation that visualizes it sharply. Plotting $\min\{Np(x_i), 1\}$, namely the contribution of x_i to effective count, accomplishes that. In Fig. 4 we color-code this input (on a logarithmic scale) and show its typical behavior on a plane containing the global probability maximum. The black regions mark the core. The panels represent different λ -regimes on the same glue background. The bulk

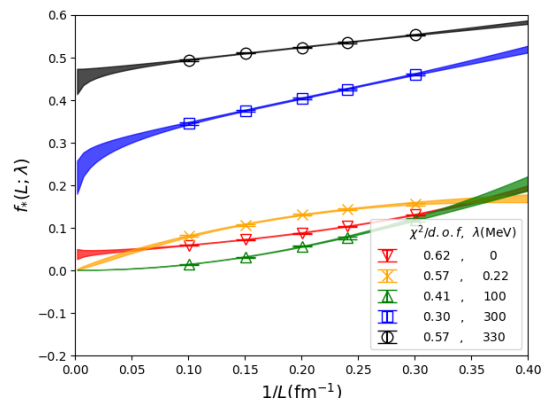


FIG. 3. Function $f_*(L)$ for various λ at $T = 234$ MeV.

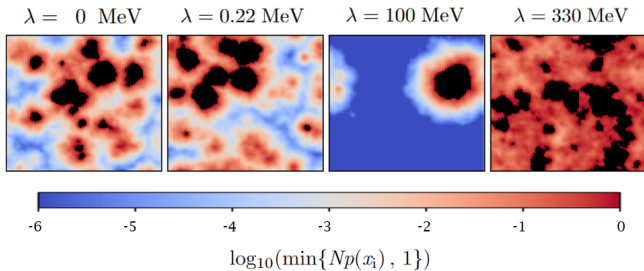


FIG. 4. Typical color-coded $\log_{10}(\min\{Np(x_i), 1\})$ in a 2d plane containing x_i with maximal probability. Modes in different λ -regimes are shown at $T=234$ MeV and $L=10.1$ fm.

mode at $\lambda = 330$ MeV (right) resembles modes at low temperatures in that its core spreads out contiguously over large distances and its granularity (composition from distinct lumps) is not very obvious. To the contrary, the plateau mode ($\lambda = 100$ MeV) is usually dominated by a well-formed lump as shown. The near-zero modes ($\lambda = 0.22$ MeV) maintain the granularity, but involve multiple lumpy features forming a larger spatial structure. The zero-modes (left) at this volume are in fact quite similar but, due to $d_{\text{IR}}=3$ vs $d_{\text{IR}}=2$ difference, will become infinitely more “space-filling” in thermodynamic limit.

Additional results are described in Appendices B,C.

5. Summary and Discussion: Remarkable property of QCD IR phase [12] is that it requires the presence of non-analyticities not only at the transition point T_{IR} , but at any temperature within the phase. It was proposed and verified [15, 16] that in pure-gluon QCD the system arranges for this by reconfiguring itself into two independent components (IR & bulk), sharply separated in Dirac spectrum. The needed non-analyticity enters via Anderson-like mobility edges $\lambda_{\text{IR}} = 0$ and $\pm\lambda_A \neq 0$, encoded by the dimension function $d_{\text{IR}}(\lambda)$. In this work we presented results suggesting that key elements of this scenario also materialize in “real-world” QCD at $T = 234$ MeV. Thus, in certain regards, thermal state in IR phase of strong interactions resembles the Tisza-Landau two-fluid model of liquid helium. The proposed 2-component nature of thermal state may in fact be the most essential attribute of IR phase.

The above is based on our results from simulations of $N_f = 2+1$ QCD at physical quark masses, UV cutoff $a = 0.105$ fm and temperatures $T = 234$ and 187 MeV. The former temperature is in the range where the transition temperature T_{IR} was originally estimated ($200 < T_{\text{IR}} < 250$ MeV) and our results suggest that $T = 234$ MeV is past that onset. Indeed, here the computed IR-dimension function $d_{\text{IR}}(\lambda)$ exhibits the same broad features as that of pure-gluon QCD in IR phase. Particularly striking is the clear presence of the identical tell-tale discontinuity at $\lambda = 0$, wherein exact zero modes ($d_{\text{IR}}(0) = 3$) are dimensionally different from lowest near-zero modes ($d_{\text{IR}}(0^+) \simeq 2$). Few aspects of our results at $T = 234$ MeV should be pointed out. (i) The computed dimension d_{IR} of near-zero modes is in close vicinity of “topological-value” 2, thus inviting a systematic inquiry into its possible origin in a certain topological feature of underlying

glue fields. At the same time, recent findings of possible topological behavior in 3d Anderson model [30] also involve dimension 2 but no glue fields. (ii) In the existing QCD data there is no clear evidence yet for critical value $d_{\text{IR}} \approx 8/3$, which was suggested to be a generic feature of Anderson models [28]. (iii) Unlike in the case of λ_{IR} , we did not find an obvious dimension jump in the vicinity of λ_A . This differs from the situation in pure-gluon QCD [15] and from that at critical points of Anderson models [28]. Taken together, points (i-iii) constitute an intriguing complex puzzle to be solved by future studies.

In contrast to $T = 234$ MeV, we found that the characteristic $\lambda = 0$ discontinuity is absent at $T = 187$ MeV. This is consistent with the original IR-phase proposal [12], wherein there is a regime of rapid but analytic change between the crossover temperature $T_A \approx T_c \approx 155$ MeV and the onset T_{IR} of IR phase. Nevertheless, as evidenced by Fig. 2, there is a dimensional structure above the deep IR and below T , which is neither low- d_{IR} plateau as in IR phase, but also not a constant $d_{\text{IR}} = 3$ as at low temperatures. Resolving its nature will require better control over both IR and UV cutoff systematics, which can be non-trivial in dynamical simulations [46] but achievable by current computational means. Some aspects of cutoff effects are discussed in Appendix D.

Recently a number of lattice QCD papers focused on the same temperature range as the one investigated here (see e.g. [47–53]). Their physics goals are mostly different and tend to involve the chiral limit, such as in studies of $U_A(1)$ problem or chiral phase transition. From symmetries perspective, it would be interesting to study how low dimensional nature of low-lying Dirac modes in IR phase relates to the approximate color-spin symmetry observed in Refs. [54, 55]. Other related developments can be found in Refs. [56–58]. The present CLQCD data could be used to study some of these problems.

ACKNOWLEDGMENTS

We thank the CLQCD collaborations for providing us their gauge configurations with dynamical fermions [31], which are generated on HPC Cluster of ITP-CAS, the Southern Nuclear Science Computing Center(SNSC) and the Siyuan-1 cluster supported by the Center for High Performance Computing at Shanghai Jiao Tong University. We also thank RBC collaborations for providing their gauge configurations, and Ting-Wai Chiu, Heng-Tong Ding and Jian Liang for valuable discussions. This work is supported in part by NSFC grants No. 12293060, 12293062, 12293065 and 12047503, a NSFC-DFG joint grant under Grant No. 12061131006 and SCHA 458/22, and also the Strategic Priority Research Program of Chinese Academy of Sciences, Grant No. XDB34030300 and YSBR-101. This work is also supported in part by the U.S. DOE Grant No. DE-SC0013065, DOE Grant No. DE-FG02-95ER40907, and DOE Grant No. DE-AC05-06OR23177 which is within

the framework of the TMD Topical Collaboration. This publication received funding from the French National Research Agency under the contract ANR-20-CE31-0016. The numerical calculation were carried out on the ORISE Supercomputer through HIP programming model [59], and HPC Cluster of ITP-CAS. This research used resources of the Oak Ridge Leadership Computing Facility at the Oak Ridge National Laboratory, which is supported by the Office of Science of the U.S. Department of Energy under Contract No. DE-AC05-

00OR22725. This work used Stampede time under the Extreme Science and Engineering Discovery Environment (XSEDE), which is supported by National Science Foundation Grant No. ACI-1053575. We also thank the National Energy Research Scientific Computing Center (NERSC) for providing HPC resources that have contributed to the research results reported within this paper. We acknowledge the facilities of the USQCD Collaboration used for this research in part, which are funded by the Office of Science of the U.S. Department of Energy.

Appendix A: Accuracy of Overlap Eigenmodes

In this section we focus on the accuracy of the low-lying eigenvectors used in this study. For efficiency reasons, we compute the low-lying eigenvalues and eigenvectors of $M \equiv \frac{1}{\rho^2} D_{\text{ov}}^\dagger D_{\text{ov}} = \frac{1}{\rho} (D_{\text{ov}} + D_{\text{ov}}^\dagger)$ in the chiral sector of exact zero mode(s). The eigenvalues and eigenvectors of D are simply related to the eigenvectors of M : non-zero modes of D_{ov} come in pairs, $\lambda_R \pm i\lambda_I$, and they span an invariant two-dimensional space for M with $\lambda_M = \lambda_R$ and for near zero-modes $\lambda_R \approx \lambda_I^2/(2\rho)$. When computing the spectrum of M , zero modes appear as Ritz pairs with eigenvalues of the order of ϵ , the precision of the sign-function approximation used to implement D_{ov} . When we have near-zero modes with $(a\lambda_I)^2 < \epsilon$, it is impossible to distinguish them from zero modes. Using a polynomial approximation for the sign functions, the best precision we are able to achieve is $\epsilon \approx 10^{-12}$, and consequently we can only confidently resolve eigenvalues with $a\lambda_I > 10^{-6}$, which in physical units correspond to $\lambda_I > 2 \times 10^{-6}$ MeV. For the volumes used in this study, the near-zero eigenmodes satisfy this condition.

Another concern is the mixing between nearly-degenerate eigenvectors. For eigenvector observables (like f_\star) that are smooth as a function of λ , this is less of a concern. However, at discontinuities mixing could introduce systematic effects. This could potentially be a problem at $\lambda = 0$ since the zero modes and near-zero modes behave differently. We argue here that this is not the case.

To see this, consider two eigenvectors of the projected operator D with $Dv_1 = i\lambda_1 v_1$ and $Dv_2 = i\lambda_2 v_2$. A mixed vector $v = v_1 \cos \theta + v_2 \sin \theta$ has a Ritz “eigenvalue” $i\lambda = v^\dagger Dv$ and residue $\delta = \|Dv - i\lambda v\| = |\cos \theta \sin \theta (\lambda_1 - \lambda_2)|$. The case relevant for us is $\lambda_1 \approx 0$ and the near-zero value $\lambda_2 > 0.1$ MeV where our residues, even in the worst case, are $\delta < 10^{-7}$. This implies that the mixing angle is at most $\theta \sim \delta/(\lambda_2 a) < 2 \times 10^{-3}$. Given that f_\star varies slowly (the difference between zero modes and near-zero modes is less than two), this mixing will have negligible effect given our statistical errors.

Appendix B: Fitting of Effective Fractions

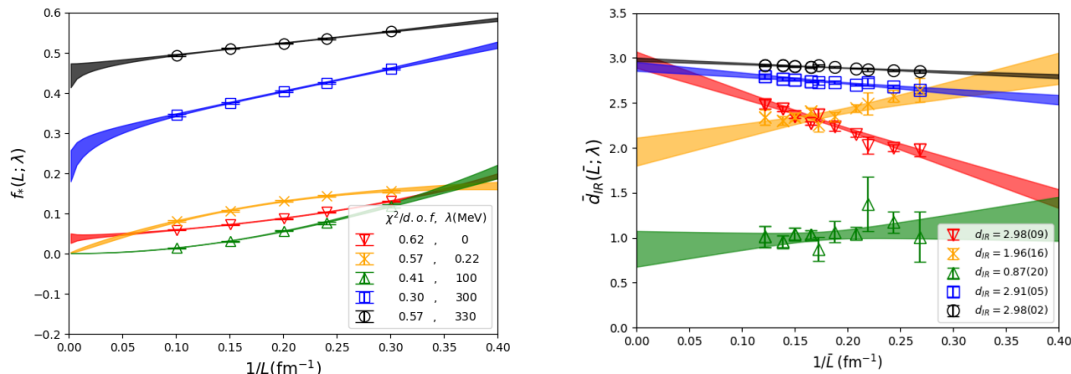


FIG. 5. Function $f_\star(L)$ (left) and the associated $\bar{d}_{\text{IR}}(\bar{L})$ (right) for various λ at $T=234$ MeV. See text for explanations.

Our procedure to extract d_{IR} assumes an approximately linear (in $1/L$) approach of “finite-volume” dimension $d_{\text{IR}}(L, s)$ in Eq. (4) to its $L \rightarrow \infty$ limit. This was suggested by Ref. [28] in the context of Anderson models. One can easily check that this is equivalent to direct fits of $\mathcal{N}_\star(L)$ to the form $\mathcal{N}_\star(L) \propto L^{d_{\text{IR}}} e^{-c/L}$ and $f_\star(L) \propto L^{d_{\text{IR}}-3} e^{-c/L}$ for effective volume fraction $f_\star(L) \equiv \mathcal{N}_\star(L)/N$. Fits shown in the left panel of Fig. 5 support the validity of this approach.

Here we wish to check the nature of finite- L correction more directly. Given the above scaling form, L -dependence of IR dimension can be expressed as

$$d_{\text{IR}}(L, s) = d_{\text{IR}} + \frac{s-1}{\ln(s)} \frac{c}{L} \quad \longrightarrow \quad \bar{d}_{\text{IR}}(\bar{L}) = d_{\text{IR}} + \frac{c}{\bar{L}} \quad \text{with} \quad \bar{d}_{\text{IR}}(\bar{L}(L, s)) \equiv d_{\text{IR}}(L, s) \quad , \quad \bar{L}(L, s) \equiv L \frac{\ln(s)}{s-1} \quad (\text{B1})$$

Introduction of variable \bar{L} thus makes it possible to combine d_{IR} results from all pairs of distinct lattices and follow their trends. Indeed, according to the above, value $\bar{d}_{\text{IR}}(1/\bar{L})$ from each pair should fall on an indicated straight line, at least near $1/\bar{L}=0$. To check this, we show in the left plot of Fig. 5 our f_* data for five largest volumes at selected values of λ , and in the right plot the associated functions $\bar{d}_{\text{IR}}(1/\bar{L})$. Note that there are 10 data points for each λ in the latter case since this is the number of possible lattice pairs. Displayed fits are indeed consistent with linear nature of $d_{\text{IR}}(1/\bar{L})$ near $1/\bar{L}=0$. The qualitative difference between exact zero modes and lowest near-zero modes is expressed in the right plot by the crossed lines representing $\lambda=0$ and $\lambda=0.22$ MeV. Their finite-volume corrections are in fact of opposite sign.

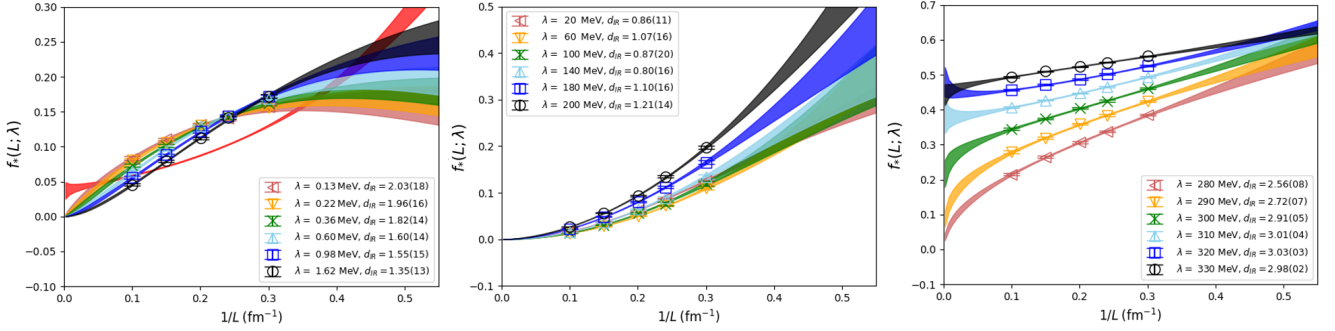


FIG. 6. Function $f_*(L)$ with different simulated size L at $T=234$ MeV, for $\lambda \in [0.1, 2.0]$ MeV (left), $\lambda \in [20, 200]$ MeV (middle) and $\lambda \in [280, 330]$ MeV (right).

We also provide the $f_*(1/L; \lambda)$ data for more values of λ in Fig. 6. As shown in the left panel, the $f_*(L > 4 \text{ fm}; 0 < \lambda < 2 \text{ MeV})$ becomes higher when λ is smaller, and thus the corresponding d_{IR} is also larger. The tendency converges at $\lambda \sim 0.2$ MeV (orange band), which corresponds to $d_{\text{IR}} = 2$ and is consistent with the $\lambda = 0.13$ MeV case (dark red band) within the uncertainty. However, this limit is significantly different from $f_*(; 0)$ as illustrated by the red band. Thus, f_* and also d_{IR} will be discontinued at $\lambda = 0$.

In contrast, the middle panel of Fig. 6 shows that d_{IR} changes smoothly with λ for $\lambda \in [20, 200]$ MeV, corresponding to $d_{\text{IR}} \sim 1$ within 2σ . The change of d_{IR} is also smooth in the range $\lambda \in [280, 330]$ MeV where it converges to 3 with increasing λ , as in the right panel. Therefore the discontinuity of d_{IR} would only occur at $\lambda = 0$, given our statistical precision at $a = 0.105$ fm and $T = 234$ MeV.

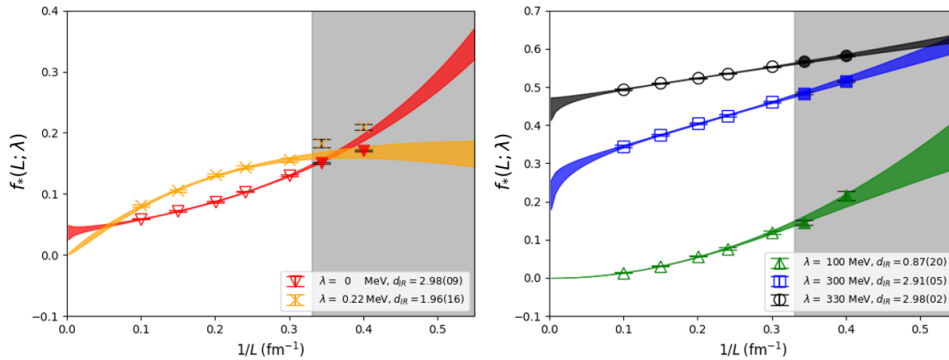


FIG. 7. Function $f_*(L)$ at $T=234$ MeV in different spectral regions, for all simulated sizes L . Left: zero modes and near-zero modes. Right: plateau, just below λ_A and at the bottom of the bulk. Shaded regions are excluded from the displayed fits.

Finally, we give a justification for using the five largest lattices in our fits i.e. systems with $L > 3$ fm. To that end, we show in Fig. 7 functions $f_*(1/L)$ for all simulated volumes, together with previously shown fits. Shaded areas

mark the volumes excluded from these fits. One can see that in case of zero modes and near-zero modes (left plot), the systems in shaded region do not follow the fit curves, and were thus excluded from fits in all spectral regions.

A similar plot of the results for $N_f = 2 + 1$ zero-temperature ensembles at $a = 0.194$ fm and $L \in \{5.7, 6.2, 9.3\}$ fm is shown in Fig. 8 (left panel). Note that f_* of exact zero modes is significantly different from that of non-zero modes, while d_{IR} is consistent with 3 at all studied values of λ .

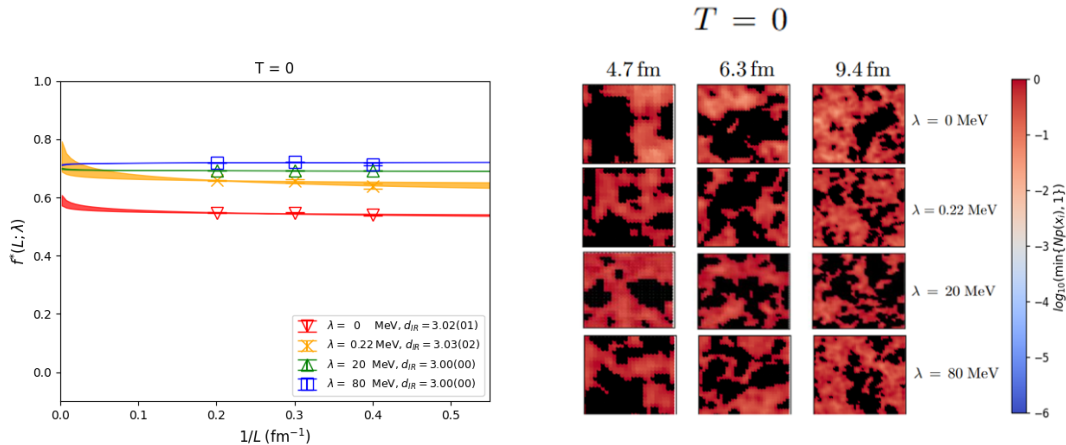


FIG. 8. $f_*(L)$ (left) and Typical color-coded $\log_{10}(\min\{Np(x_i), 1\})$ in a 2d plane containing point x_i with maximal probability (right) at zero temperature.

Appendix C: Visualization of Spatial Distributions

In this Appendix we wish to extend our visualization of mode distributions in various λ -regimes at $T = 234$ MeV shown in Fig. 4 of the manuscript.

In particular, the right panel of Fig. 8 demonstrates that zero-temperature mode distributions remain quite similar at different scales λ and various IR cutoffs, and are qualitatively different from that shown in Fig. 4.

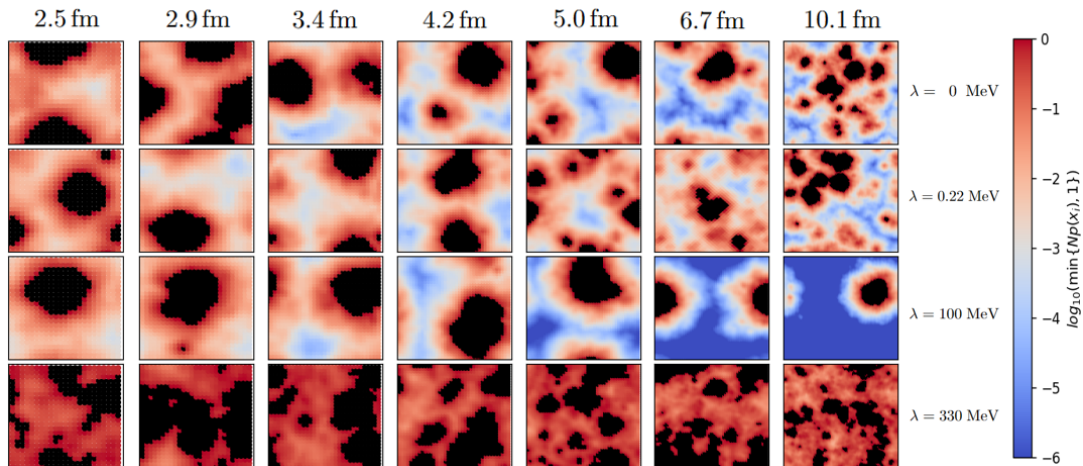


FIG. 9. Typical color-coded $\log_{10}(\min\{Np(x_i), 1\})$ in a 2d plane containing point x_i with maximal probability. Modes in different λ -regimes on a given glue background at $T=234$ MeV are shown for all spatial sizes L studied.

In contrast, Fig. 9 shows examples of modes at the same four values of λ , but at all IR cutoffs (sizes L of the system) considered in this work. for $T=234$ MeV. Note that $\lambda=0, 0.22$ and 100 MeV belong to the IR part of the spectrum, while $\lambda=330$ MeV is in a near-bottom part of the bulk.

Interesting aspect of observing the typical geometry at fixed λ for increasing L is an evolution in degree of granularity. Indeed, note that for the plateau mode ($\lambda=100$ MeV), increasing L confirms the picture of a single solid lump present in the volume. On the other hand, for zero-modes and near-zero modes, the apparent (visually observable) degree of granularity increases with increasing L , reflecting that their effective supports keeps spreading out in the volume. In

TABLE II. UV cutoff a , pion mass m_π , lattice volumes $n_L^3 \times n_T$ and temperature T of lattice QCD ensembles studied.

$a(\text{fm})$	$m_\pi(\text{MeV})$	n_L	n_T	$T(\text{MeV})$	
0.105	135	24/28/32/40/48/64/96	8	234	
		32/40/48/64	10	187	
0.105	290	24	8	234	
0.052	317	48/	96	16	234

fact, all qualitative aspects we observe agree with metal-to-critical picture of transition to IR phase, put forward in Ref. [16]. The associated details will be worked out in dedicated follow-up publications.

Appendix D: Lattice Spacing Dependence

To assess the impact of lattice spacing on our findings, we recalculated $\rho(\lambda)$ and f_\star at $a = 0.052$ fm with a heavier pion mass of $m_\pi = 317$ MeV, and also $\rho(\lambda)$ at $a = 0.105$ fm with $m_\pi = 290$ MeV. Details regarding these ensembles are listed in Table II.

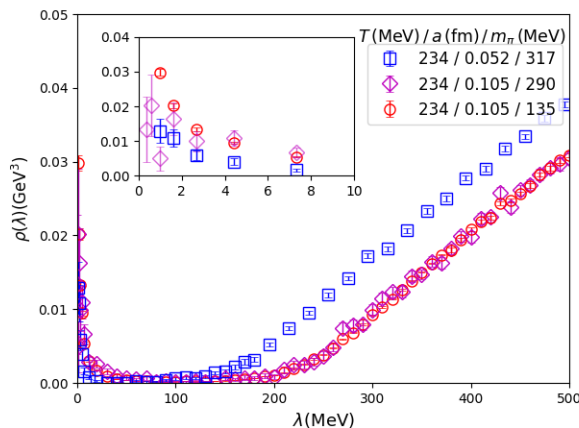


FIG. 10. Spectral density $\rho(\lambda)$ at $T = 234$ MeV at $a = 0.105$ fm with $m_\pi = 135$ MeV (red dots), $m_\pi = 290$ MeV (pink diamonds), and $a = 0.052$ fm with $m_\pi = 317$ MeV (blue crosses).

In Fig. 10, pink diamonds show the $\rho(\lambda)$ at $a = 0.105$ fm with $m_\pi = 290$ MeV with relatively low statistics, and show good consistency with that at the same lattice spacing but $m_\pi = 135$ MeV (red dots). It suggests that the pion mass dependence of $\rho(\lambda)$ is weak, as shown in the previous study using the overlap fermion on the Domain wall sea [49]. Thus we calculate $\rho(\lambda)$ at smaller lattice spacing but heavier pion mass to investigate the lattice spacing dependence.

As shown as the blue crosses in Fig. 10, the peak of $\rho(\lambda)$ at small λ diminishes at $a = 0.052$ fm with the same temperature but a heavier m_π . This decrease implies that the magnitude of this peak may contain a significant discretization error, such as the mixed action effect. At the same time, $\rho(\lambda)$ at $a = 0.052$ fm becomes higher than that at $a = 0.105$ fm for $\lambda > 120$ MeV. This disparity is also likely primarily attributed to discretization errors.

Regarding f_\star , we display the f_\star values at two temperatures and $a = 0.105$ fm in Fig. 11 for various typical λ , and include the values at $T = 234$ MeV and $a = 0.052$ fm (blue boxes) for two volumes for comparison. The values at $a = 0.052$ fm are typically lower than those at $a = 0.105$ fm for $\lambda < 100$ MeV, indicating a sparse distribution in the infinite volume limit. However, f_\star are larger for $\lambda > 100$ MeV, which can result in a decrease in λ_A such that $d_{\text{IR}}(\lambda > \lambda_A) = 3$ as we approach the continuum limit.

In addition, comparing the f_\star with two temperatures at $a = 0.105$ fm, those at higher temperature are always lower and suggest that the Dirac mode and then gluon field become “sparser”.

[1] R. Hagedorn, Nuovo Cim. Suppl. **3**, 147 (1965).

[2] R. Hagedorn, CERN report 71-12 (1971), 10.5170/CERN-1971-012.

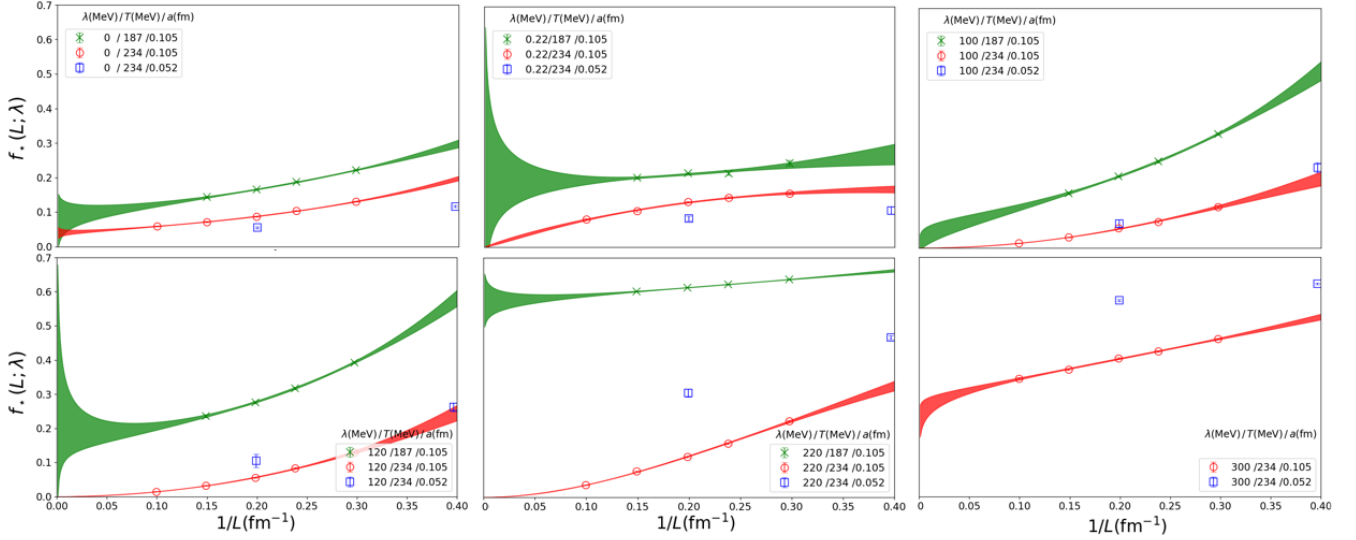


FIG. 11. Function $f_*(1/L)$ for various values of λ , temperatures and UV cutoffs.

- [3] L. D. McLerran and B. Svetitsky, Phys. Lett. B **98**, 195 (1981).
- [4] J. Kuti, J. Polonyi, and K. Szlachanyi, Phys. Lett. B **98**, 199 (1981).
- [5] J. Engels, F. Karsch, H. Satz, and I. Montvay, Phys. Lett. B **101**, 89 (1981).
- [6] Y. Aoki, G. Endrodi, Z. Fodor, S. Katz, and K. Szabo, Nature **443**, 675 (2006), arXiv:hep-lat/0611014 [hep-lat].
- [7] I. Arsene et al. (BRAHMS), Nucl. Phys. **A757**, 1 (2005), arXiv:nucl-ex/0410020 [nucl-ex].
- [8] B. B. Back et al., Nucl. Phys. **A757**, 28 (2005).
- [9] J. Adams et al. (STAR), Nucl. Phys. **A757**, 102 (2005), arXiv:nucl-ex/0501009 [nucl-ex].
- [10] K. Adcox et al. (PHENIX), Nucl. Phys. **A757**, 184 (2005), arXiv:nucl-ex/0410003 [nucl-ex].
- [11] B. Muller, J. Schukraft, and B. Wyslouch, Ann. Rev. Nucl. Part. Sci. **62**, 361 (2012), arXiv:1202.3233 [hep-ex].
- [12] A. Alexandru and I. Horváth, Phys. Rev. D **100**, 094507 (2019), arXiv:1906.08047 [hep-lat].
- [13] R. G. Edwards, U. M. Heller, J. E. Kiskis, and R. Narayanan, Phys. Rev. **D61**, 074504 (2000), arXiv:hep-lat/9910041 [hep-lat].
- [14] A. Alexandru and I. Horváth, Phys. Rev. **D92**, 045038 (2015), arXiv:1502.07732 [hep-lat].
- [15] A. Alexandru and I. Horváth, Phys. Rev. Lett. **127**, 052303 (2021), arXiv:2103.05607 [hep-lat].
- [16] A. Alexandru and I. Horváth, Phys. Lett. B **833**, 137370 (2022), arXiv:2110.04833 [hep-lat].
- [17] A. M. Garcia-Garcia and J. C. Osborn, Nucl. Phys. A **770**, 141 (2006), arXiv:hep-lat/0512025.
- [18] A. M. Garcia-Garcia and J. C. Osborn, Phys. Rev. D **75**, 034503 (2007), arXiv:hep-lat/0611019.
- [19] T. G. Kovacs and F. Pittler, Phys. Rev. Lett. **105**, 192001 (2010), arXiv:1006.1205 [hep-lat].
- [20] M. Giordano, T. G. Kovacs, and F. Pittler, Phys. Rev. Lett. **112**, 102002 (2014), arXiv:1312.1179 [hep-lat].
- [21] L. Ujfalusi, M. Giordano, F. Pittler, T. G. Kovács, and I. Varga, Phys. Rev. D **92**, 094513 (2015), arXiv:1507.02162 [cond-mat.dis-nn].
- [22] I. Horváth, P. Markoš, and R. Mendris, Entropy **25**, 482 (2023), arXiv:2205.11520 [hep-lat].
- [23] I. Horváth and R. Mendris, Entropy **22**, 1273 (2020), arXiv:1807.03995 [quant-ph].
- [24] I. Horváth, Quantum Rep. **3**, 534 (2021), arXiv:1809.07249 [quant-ph].
- [25] I. Horváth and R. Mendris, MDPI Proc. **13**, 8 (2019), arXiv:1907.01606 [quant-ph].
- [26] R. A. Vig and T. G. Kovacs, Phys. Rev. D **103**, 114510 (2021), arXiv:2101.01498 [hep-lat].
- [27] M. Cardinali, M. D'Elia, and A. Pasqui, (2021), arXiv:2107.02745 [hep-lat].
- [28] I. Horváth and P. Markoš, Phys. Rev. Lett. **129**, 106601 (2022), arXiv:2110.11266 [cond-mat.dis-nn].
- [29] I. Horváth and P. Markoš, Phys. Lett. A **467**, 128735 (2023), arXiv:2207.13569 [cond-mat.dis-nn].
- [30] I. Horváth and P. Markoš, (2022), arXiv:2212.09806 [cond-mat.dis-nn].
- [31] Z.-C. Hu et al. (CLQCD), Phys. Rev. D **109**, 054507 (2024), arXiv:2310.00814 [hep-lat].
- [32] Q.-A. Zhang, J. Hua, F. Huang, R. Li, Y. Li, C.-D. Lu, P. Sun, W. Sun, W. Wang, and Y.-B. Yang, (2021), arXiv:2103.07064 [hep-lat].
- [33] H. Liu, J. He, L. Liu, P. Sun, W. Wang, Y.-B. Yang, and Q.-A. Zhang, (2022), arXiv:2207.00183 [hep-lat].
- [34] H. Xing, J. Liang, L. Liu, P. Sun, and Y.-B. Yang, (2022), arXiv:2210.08555 [hep-lat].
- [35] H. Liu, L. Liu, P. Sun, W. Sun, J.-X. Tan, W. Wang, Y.-B. Yang, and Q.-A. Zhang, (2023), arXiv:2303.17865 [hep-lat].
- [36] H. Neuberger, Phys. Lett. **B417**, 141 (1998), arXiv:hep-lat/9707022 [hep-lat].
- [37] D. C. Sorensen, SIAM J. on Matrix Analysis and Applications **13**, 357 (1992).
- [38] R. B. Lehoucq and D. C. Sorensen, SIAM J. Matrix Anal. Appl. **17**, 789 (1996).
- [39] L. Giusti, C. Hoelbling, M. Luscher, and H. Wittig, Comput. Phys. Commun. **153**, 31 (2003), arXiv:hep-lat/0212012 [hep-lat].

- [40] A. Alexandru, M. Lujan, C. Pelissier, B. Gamari, and F. X. Lee, in *Proceedings, SAAHPC'11* (2011) pp. 123–130, arXiv:1106.4964 [hep-lat].
- [41] T.-W. Chiu and S. V. Zenkin, *Phys. Rev.* **D59**, 074501 (1999), arXiv:hep-lat/9806019 [hep-lat].
- [42] F. He, Y.-J. Bi, T. Draper, K.-F. Liu, Z. Liu, and Y.-B. Yang (χ QCD), *Phys. Rev. D* **106**, 114506 (2022), arXiv:2204.09246 [hep-lat].
- [43] G. Cossu, H. Fukaya, S. Hashimoto, T. Kaneko, and J.-I. Noaki, *PTEP* **2016**, 093B06 (2016), arXiv:1607.01099 [hep-lat].
- [44] R. Arthur et al. (RBC, UKQCD), *Phys. Rev. D* **87**, 094514 (2013), arXiv:1208.4412 [hep-lat].
- [45] P. Boyle et al., *Phys. Rev. D* **93**, 054502 (2016), arXiv:1511.01950 [hep-lat].
- [46] D.-J. Zhao, G. Wang, F. He, L. Jin, P. Sun, Y.-B. Yang, and K. Zhang (χ QCD), *Phys. Rev. D* **107**, L091501 (2023), arXiv:2207.14132 [hep-lat].
- [47] V. Dick, F. Karsch, E. Laermann, S. Mukherjee, and S. Sharma, *Phys. Rev.* **D91**, 094504 (2015).
- [48] H. T. Ding, S. T. Li, S. Mukherjee, A. Tomiya, X. D. Wang, and Y. Zhang, (2020), arXiv:2010.14836 [hep-lat].
- [49] S. Aoki, Y. Aoki, G. Cossu, H. Fukaya, S. Hashimoto, T. Kaneko, C. Rohrhofer, and K. Suzuki (JLQCD), *Phys. Rev. D* **103**, 074506 (2021), arXiv:2011.01499 [hep-lat].
- [50] O. Kaczmarek, L. Mazur, and S. Sharma, *Phys. Rev. D* **104**, 094518 (2021).
- [51] A. Y. Kotov, M. P. Lombardo, and A. Trunin, *Physics Letters B* **823**, 136749 (2021).
- [52] Y.-C. Chen, T.-W. Chiu, and T.-H. Hsieh (TWQCD), *Phys. Rev. D* **106**, 074501 (2022), arXiv:2204.01556 [hep-lat].
- [53] O. Kaczmarek, R. Shanker, and S. Sharma, (2023), arXiv:2301.11610 [hep-lat].
- [54] C. Rohrhofer, Y. Aoki, G. Cossu, H. Fukaya, C. Gattringer, L. Ya. Glozman, S. Hashimoto, C. B. Lang, and S. Prelovsek, *Phys. Rev.* **D100**, 014502 (2019).
- [55] L. Y. Glozman, O. Philipsen, and R. D. Pisarski, *Eur. Phys. J. A* **58**, 247 (2022), arXiv:2204.05083 [hep-ph].
- [56] K.-F. Liu, (2023), arXiv:2302.11600 [hep-ph].
- [57] A. Athenodorou, C. Bonanno, C. Bonati, G. Clemente, F. D'Angelo, M. D'Elia, L. Maio, G. Martinelli, F. Sanfilippo, and A. Todaro, *JHEP* **10**, 197 (2022), arXiv:2208.08921 [hep-lat].
- [58] R. Kehr, D. Smith, and L. von Smekal, (2023), arXiv:2304.13617 [hep-lat].
- [59] Y.-J. Bi, Y. Xiao, W.-Y. Guo, M. Gong, P. Sun, S. Xu, and Y.-B. Yang, *Proceedings, Lattice 2019, PoS LATTICE2019*, 286 (2020), arXiv:2001.05706 [hep-lat].